

A Thermo-electromagnetically Actuated Microrobot for the Targeted Transport of Therapeutic Agents

Gwangjun Go, Van Du Nguyen, Zhen Jin, Jong-Oh Park*, and Sukho Park*

Abstract: This work proposes the targeted transport of therapeutic agents using a thermo-electromagnetically actuated microrobot. This microrobot is fabricated via UV polymerization using 2D lithography and is composed of an electromagnetically actuated layer (polyethyleneglycol diacrylate dispersed with iron(II,III) oxide and a thermo-responsive layer (N-isopropylacrylamide). The microrobot can self-fold, driven by temperature changes, and can be steered using an electromagnetic actuation (EMA) system that provides external magnetic fields. In particular, during the EMA, pulling and rolling motions are applied to the unfolded and folded shapes, respectively, of the microrobot. As fundamental tests, the microrobot was characterized in terms of its magnetization curve, swelling properties, travel velocity, and shape changing behavior. In addition, typical polystyrene bead manipulations such as trapping, delivery, and release were performed using the microrobot. Finally, we performed an in vitro test for tumor therapy, in which the robot demonstrated the ability to trap, deliver, and release an anti-cancer drug (docetaxel) encapsulated in microbeads of approximately 300 μm in diameter with an appropriate drug concentration against a mouse mammary tumor cell line (4T1). The outcomes of this research suggest that our thermo-electromagnetically actuated microrobot is suitable for use in biomedical applications.

Keywords: Bilayer structure, electromagnetic field control, hybrid actuated microrobot, thermally responsive hydrogel.

1. INTRODUCTION

Recently, various types of wireless microrobots have been developed for use in bioengineering and healthcare applications [1–3]. Compared to general surgical operations, because milli/micrometer-scale robots can approach small and complex regions of the human body (such as inside the eyeball, the blood and lymphatic capillaries, the hepatic artery, and biological tissues and cells), they can perform non-invasive or minimally invasive surgery. For microrobots to be suitable for use in biomedical applications, after the microrobots fulfill their functions, such as transport, diagnosis, and therapy, they should spontaneously degrade or be rescued from the target regions. In addition, for the safety of normal tissues and cells, biocompatible materials must be used in microrobot fabrication.

As a representative means of microrobot locomotion, electromagnetic actuation (EMA) has attracted consider-

able attention. Because EMA enables the wireless control of microrobots, minimally invasive target manipulations using microrobots are possible. Moreover, due to the fine control that can be exerted over the magnetic field generated using EMA, the microrobots can freely move on a 2D plane or in 3D space. By virtue of the advantages of using an external electromagnetic field, many microrobots with diverse motions, such as pulling [4], rolling [5, 6], gripping [7], swimming [8, 9], oscillating [10, 11], and stick-slip [12] motions, have been reported for use in biomedical applications.

More recently, new microrobots with hybrid actuation have been developed for use in biomedical applications. Here, hybrid actuation refers to EMA combined with the use of an acoustic field [13], thermal response [14–19], living organisms [20, 21], or chemical reactions [22, 23]. In particular, in the case of hybrid actuation achieved through the combination of EMA and thermal actuation, microrobots composed of magnetic and thermally respon-

Manuscript received February 1, 2017; revised June 12, 2017 and September 3, 2017; accepted November 17, 2017. Recommended by Associate Editor Huaping Liu under the direction of Editor Fuchun Sun. This work was supported by the Industrial Technology Innovation Program [10060059, Externally Actuatable Nanorobot System for Precise Targeting and Controlled Releasing of Drugs] funded by the Ministry of Trade, Industry and Energy (MOTIE, Korea).

Gwangjun Go, Van Du Nguyen, Zhen Jin, and Jong-Oh Park are with School of Mechanical Engineering, Chonnam National University, Gwangju 61186, Korea (e-mails: gwangjun124@gmail.com, nvdu81@gmail.com, jinzhen416@hotmail.com, jop@jnu.ac.kr). Gwangjun Go and Jong-Oh Park are also with Medical Microrobot Center (MRC), Robot Research Initiative (RRI), Chonnam National University, Gwangju 61186, Korea, and they are with School of Mechanical Engineering, Chonnam National University, Gwangju 61186, Korea. Sukho Park is with Department of Robotics Engineering, Daegu Gyeongbuk Institute of Science and Technology, Daegu 42988, Korea (e-mail: shpark12@dgist.ac.kr).

* Corresponding authors.

sive materials can be manipulated by an external magnetic field, and their shapes can be modified by external stimuli, such as infrared light, alternating magnetic fields, and other heating methods. For example, it has been demonstrated that drug-loaded microrobots [19] and microgrippers [14, 16, 17] operating based on thermo-electromagnetic hybrid actuation can realize more diverse and flexible motions than electromagnetically actuated microrobots with rigid bodies. Tabatabaei *et al.* proposed the use of a drug-loaded microrobot composed of thermally shrinkable N-isopropylacrylamide (NIPAAm) hydrogels containing drugs and magnetic nanoparticles (MNPs). This microrobot can realize magnetic actuation, be position tracked using a magnetic resonance imaging (MRI) system, and control drug release through shrinkage of the hydrogel by heating the MNPs using alternating magnetic fields. However, microrobots using non-biodegradable hydrogel cannot be quickly rescued from the biological environment because the microrobot should stay in the area to release drugs over long periods. Thus, such microbots can cause several side effects due to the toxicity of the MNPs and foreign body reactions. Fusco *et al.* proposed flytrap-like microrobots with a thermally actuated hydrogel bilayer. Using thermal actuation, the microrobot can trap MNPs containing therapeutic beads. Therefore, the microrobot can be manipulated to a target by magnetic actuation. However, once the MNPs containing beads are released from the microrobot, it cannot be manipulated any further by magnetic actuation. In addition, previous hybrid actuated microrobots used only a single electromagnetic actuated motion regardless of their environment and the microrobot shape. Additionally, in previous studies of hybrid actuated microrobots, the authors separately demonstrated thermal and electromagnetic actuation of the microrobot. These authors also showed only therapeutic effects using the microrobot without hybrid actuation. Therefore, no previous reports involving *in vitro* tests have simultaneously demonstrated the powerful performance provided by a hybrid (thermal and electromagnetic)-actuated microrobot and a therapeutic effect following drug delivery.

In this paper, we verified the transportation of therapeutic agents and their therapeutic effect using the thermo-electromagnetically actuated microrobot. The microrobot, which is composed of an electromagnetically actuated layer and a thermally actuated layer, is fabricated via UV polymerization. First, by means of the thermally actuated layer, the microrobot can be made to self-fold at the desired location via external thermal activation; thus, it can trap and release micro-objects carrying therapeutic agents. Next, by means of the electromagnetically actuated layer, the microrobot can be guided to its target by an EMA system. Depending on the shape of the microrobot, which changes with environmental temperature, two different motions of the microrobot can be achieved,

such as a pulling motion and a rolling motion. To demonstrate the concept of the hybrid actuated microrobot, we fabricated such a microrobot with a bilayer structure for electromagnetic and thermal actuation. The fabricated microrobot was characterized in terms of its magnetization curve, swelling ratio, travel velocity, and shape changing behavior. Using the microrobot, typical manipulations of a polystyrene bead (300 μm), including trapping, delivery, and release, were performed. Finally, an *in vitro* test for tumor therapy using the microrobot was performed. Before the *in vitro* test, drug-carrying microbeads were fabricated using the optimum drug concentration and biocompatible materials. Subsequently, the fabricated microbeads were delivered by the hybrid actuated microrobot to tumor cells, and the therapeutic effects of the delivered microbeads were observed as morphological changes in the tumor cells.

2. THE CONCEPT UNDERLYING THE TARGETED TRANSPORT OF THERAPEUTIC AGENTS USING THE HYBRID ACTUATED MICROROBOT

2.1. Thermal actuation of the microrobot

The microrobot has a bilayer structure comprising an electromagnetically actuated layer and a thermally actuated layer (Fig. 1(a)). The electromagnetically actuated layer consists of biocompatible poly(ethylene glycol) diacrylate (PEGDA) [24] dispersed with iron(II,III) oxide, and the thermally actuated layer is formed of a thermally responsive NIPAAm hydrogel. In particular, the NIPAAm hydrogel, as a biocompatible material, exhibits the valuable characteristics of a sharp phase transition and a large swelling ratio at 30-35°C; a temperature in this range is known as the lower critical solution temperature (LCST) [25, 26]. Therefore, with a decrease (or increase) in temperature, the hydrogel absorbs (or expels) water molecules, and the volume of the hydrogel swells (or shrinks). Thus, the bilayer structure opens at temperatures below the LCST, and the structure folds toward the thermally actuated layer (NIPAAm hydrogel) at temperatures above the LCST. The microrobot, with eight bending arms that operate through the bending mechanism of the bilayer structure, is designed and fabricated via two UV polymerization processes using 2D lithography (Fig. 2). The detailed fabrication procedure of the microrobot is explained in Section 3 (Materials and Methods). Through its self-folding motion, the microrobot can trap or release micro-objects carrying therapeutic agents (Fig. 1(b)). To achieve this self-folding motion of the microrobot, we introduce a heating stage combined with a Peltier element, and we modify the shape of the self-folding microrobot using the heat generated by this heating stage.

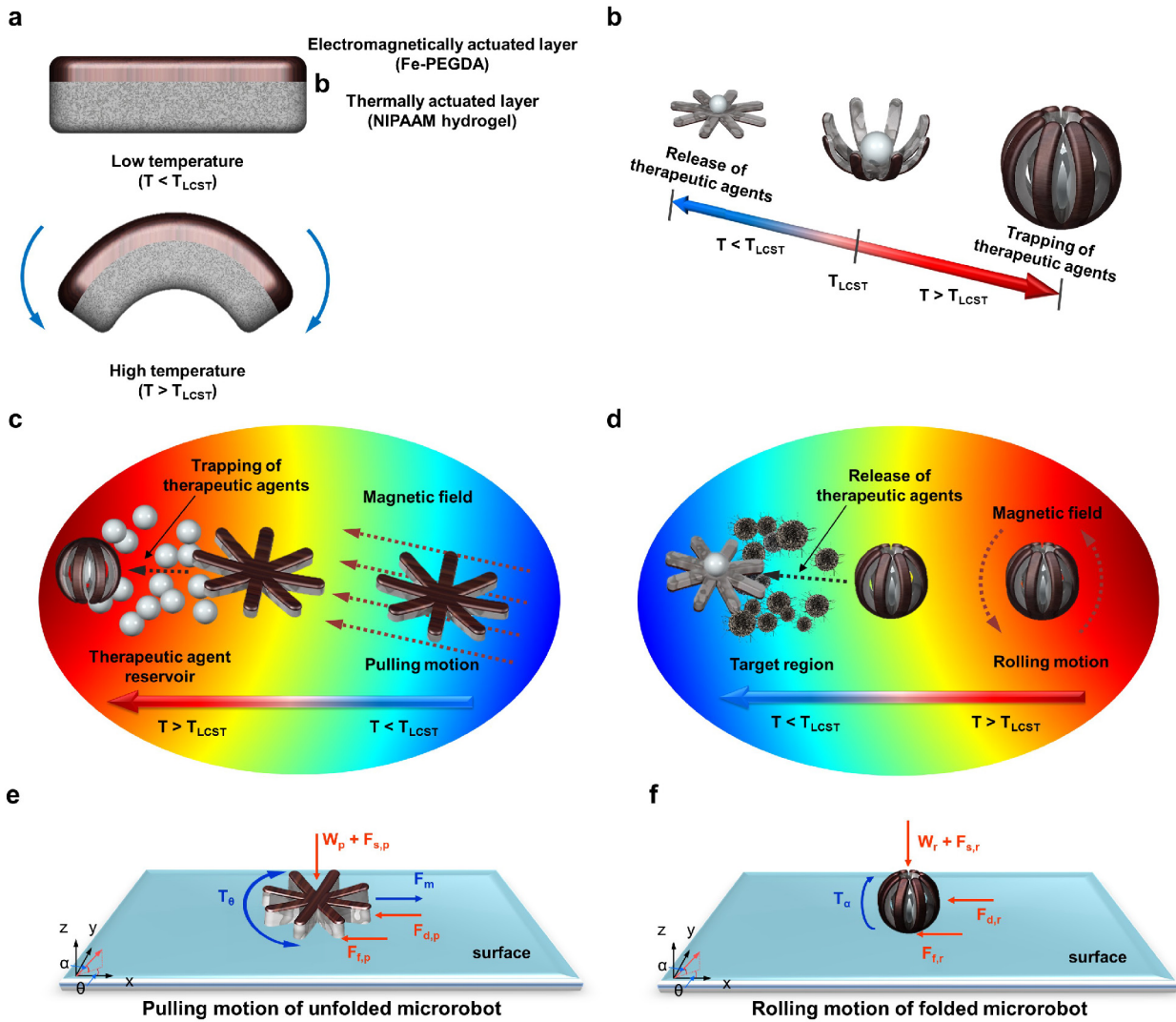


Fig. 1. Concept of the thermo-electromagnetically actuated microrobot for the targeted transport of therapeutic agents. (a) The actuation principle of the microrobot, which is composed of electromagnetically and thermally actuated layers. (b) The trapping and release of therapeutic agents by the microrobot, as controlled by changes in temperature. (c) Using a pulling motion, the microrobot is made to approach a reservoir of therapeutic agents. Then, as the temperature is increased ($T < T_{LCST}$), the microrobot folds and traps the therapeutic agents. (d) Using a rolling motion, the microrobot is made to deliver the therapeutic agents to the target region. As the temperature is decreased ($T > T_{LCST}$), the microrobot opens, and the therapeutic agents are released to the target. T and T_{LCST} represent the surrounding temperature and the lower critical solution temperature of the microrobot, respectively. (e) A free body diagram of the unfolded microrobot with pulling motion along the x -axis. T_θ , F_m , $F_{f,p}$, $F_{d,p}$, $F_{s,p}$, and W_p are the oscillating magnetic torque, pulling magnetic force, kinetic frictional force, drag force, adhesive force due to the van der Waals force and microrobot weight, respectively. (f) A free body diagram of the folded microrobot with a rolling motion along the x -axis. T_α , $F_{f,r}$, $F_{d,r}$, $F_{s,r}$, and W_r are the rotating magnetic torque, rolling frictional force, drag force, adhesive force due to the van der Waals force and microrobot weight (including the drug-loaded beads), respectively.

2.2. Electromagnetic actuation of the microrobot

The microrobot can be steered by means of an EMA system and can move freely on a 2D plane because of the inclusion of iron(II,III) oxide, a magnetic mate-

rial, in the electromagnetically actuated layer of the microrobot. To realize the locomotion of the microrobot on a 2D plane, we designed an EMA system consisting of three stationary pairs of Helmholtz coils on the x , y , and z axes and two stationary pairs of Maxwell coils on the x

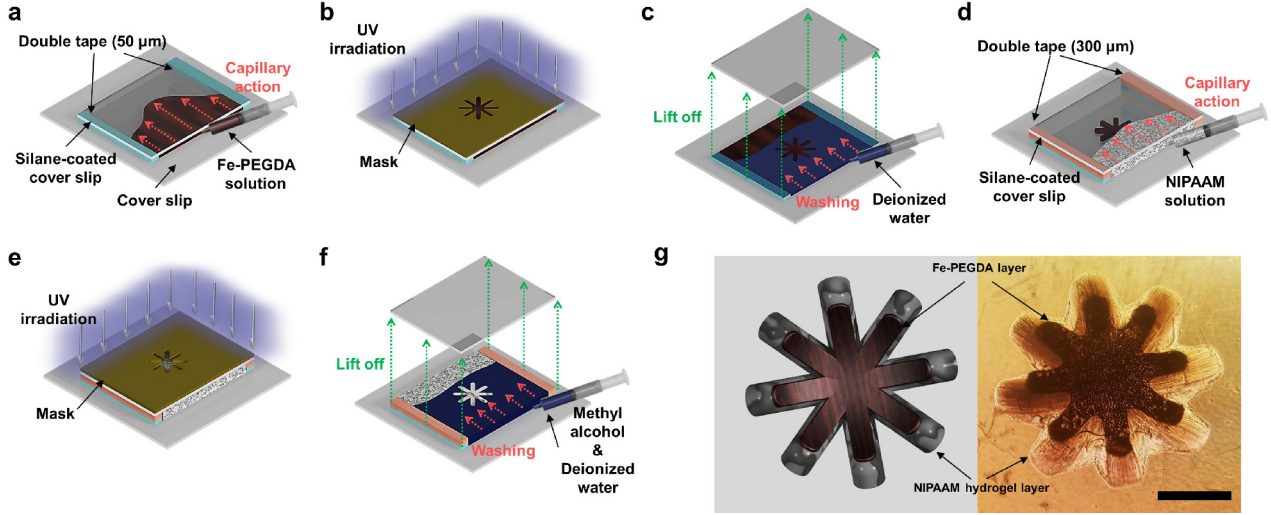


Fig. 2. Schematic diagram of the microrobot fabrication process. (a) An Fe-PEGDA solution was injected by capillary force into the channel between two coverslips, which were separated by a distance of 50 μm . (b) A photomask with the pattern of the microrobot was placed over the channel, which was then irradiated with UV light to polymerize the Fe-PEGDA solution. (c) The silane-coated upper coverslip of the channel was removed, and the non-polymerized solution in the channel was washed away by injecting additional deionized water. (d) A NIPAAM solution was injected into the channel between the two coverslips, which were separated by a distance of 350 μm . (e) After the photomask was aligned over the channel, the NIPAAM solution was polymerized under UV exposure. (f) The silane-coated upper coverslip of the channel was then removed, and the non-polymerized solution was washed away by injecting additional methyl alcohol and deionized water. (g) A CAD image and an optical micrograph of the fabricated microrobot. The scale bar represents 1 mm.

and y axes (Fig. 4). First, the Helmholtz coils generate a uniform magnetic field in the region of interest (ROI) to align the microrobot in the desired direction [27]. Once the microrobot is located in the uniform magnetic field generated by the Helmholtz coils on the x , y , and z axes, it is rotated and aligned in the direction of the generated uniform magnetic field. Therefore, the following torque ($\boldsymbol{\tau}$) is generated to align the microrobot:

$$\boldsymbol{\tau} = V\mathbf{M} \times \mathbf{B}, \quad (1)$$

where V and \mathbf{M} denote the volume and magnetization of the microrobot and \mathbf{B} denotes the magnetic flux of the external magnetic field.

Second, the Maxwell coils generate a uniform-gradient magnetic field in the ROI to propel the microrobot in the aligned direction [27]. The magnetic force (\mathbf{F}) on the microrobot from the uniform-gradient magnetic field is described as follows:

$$\mathbf{F} = V(\mathbf{M} \cdot \nabla)\mathbf{B}, \quad (2)$$

where ∇ is the gradient symbol. Using this principle of microrobot locomotion, pulling and rolling motions can be also achieved by controlling the magnetic fields generated by the EMA system, as studied in our previous works [5, 28, 29].

Fig. 1(e) and (f) show free body diagrams of the microrobot with different morphologies and motions, respectively. First, in Fig. 1(e), a pulling motion can be applied to the microrobot by means of the uniform magnetic field and the uniform gradient magnetic field that are generated by the Helmholtz and Maxwell coils, respectively. In general, the pulling motion of the microrobot on a 2D plane is affected by the frictional force between the microrobot and the bottom surface and by van der Waals forces [11, 30]. Therefore, it is difficult for the magnetic force (F_m) generated by the gradient magnetic field to overcome these forces acting on the microrobot [11]. To reduce the effect of the friction force, an oscillating magnetic torque (T_θ) generated by the Helmholtz coils on the x and y axes is applied to achieve the pulling motion of the microrobot. Due to the microrobot oscillation, a kinetic frictional force ($F_{f,p}$) acts on the microrobot instead of a static frictional force. Therefore, the oscillating magnetic field allows the microrobot to overcome the static frictional force acting on it [11]. The oscillating magnetic field on the 2D plane can be described as follows:

$$\mathbf{B} = \begin{bmatrix} B_x(t) \\ B_y(t) \end{bmatrix} = \begin{bmatrix} B_{0,p} \cos(\theta + \alpha \cos(\beta t)) \\ B_{0,p} \sin(\theta + \alpha \sin(\beta t)) \end{bmatrix}, \quad (3)$$

where $B_{0,p}$ is the magnetic flux generated by the two pairs of Helmholtz coils, and θ is the alignment angle of the mi-

crorobot. Furthermore, α and β are the oscillating angle and the angular velocity of the microrobot, respectively. In the pulling motion, the resulting propulsion direction of the microrobot is equivalent to the alignment angle (θ) of the microrobot [11, 31].

Next, during the rolling motion of the microrobot on the 2D plane (Fig. 1(f)), the microrobot experiences smaller frictional force ($F_{f,r}$) than the pulling motion. Therefore, the rolling motion of the microrobot requires a smaller magnetic field than does the pulling motion, and the microrobot can move more easily in this model [6]. The rolling motion of the microrobot using the rotating magnetic torque (T_α) is realized by the uniform magnetic field, which is generated by the three pairs of Helmholtz coils, producing a rotating magnetic field that can be described as follows:

$$\mathbf{B} = \begin{bmatrix} B_x(t) \\ B_y(t) \\ B_z(t) \end{bmatrix} = \begin{bmatrix} B_{0,r} \cos \theta \cos wt \\ B_{0,r} \sin \theta \cos wt \\ B_{0,r} \sin wt \end{bmatrix}, \quad (4)$$

where $B_{0,r}$ and w denote the magnetic flux generated in the Helmholtz coils and the rolling angular velocity of the microrobot, respectively.

The two motions (pulling and rolling) of the microrobot are selectively applied depending on the shape adopted by the microrobot due to the temperature changes (Fig. 1(b)-(f)). The unfolded shape of the microrobot at temperatures below the LCST has a larger surface area than does the shape formed by the microrobot at temperatures above the LCST. Thus, at temperatures below the LCST, the rolling motion of the unfolded microrobot is affected by a larger drag force than is the pulling motion. Hence, the pulling motion is used to control the unfolded microrobot. Once the microrobot has folded to trap the micro-objects carrying the therapeutic drug of interest, the microrobot needs to reach its target area as soon as possible to avoid the possibility that the encapsulated drugs may be released during the microrobot's motion. In addition, a folded microrobot containing trapped therapeutic agents weighs more than an unfolded microrobot ($W_r > W_p$). Therefore, for the folded microrobot at temperatures above the LCST, the rolling motion requires less energy and is more suitable than the pulling motion.

2.3. Transport of therapeutic agents using the microrobot

Based on the working principle of the microrobot, the transport process for therapeutic agents is as follows. First, a pulling motion is applied to the unfolded microrobot ($T < T_{LCST}$) to move it into the reservoir of micro-objects containing therapeutic agents. Then, the self-folding of the microrobot is activated by an external stimulus ($T > T_{LCST}$) to trap the micro-objects (Fig. 1(c)). Next, the microrobot containing the trapped micro-objects is moved into the target region using a rolling motion, and

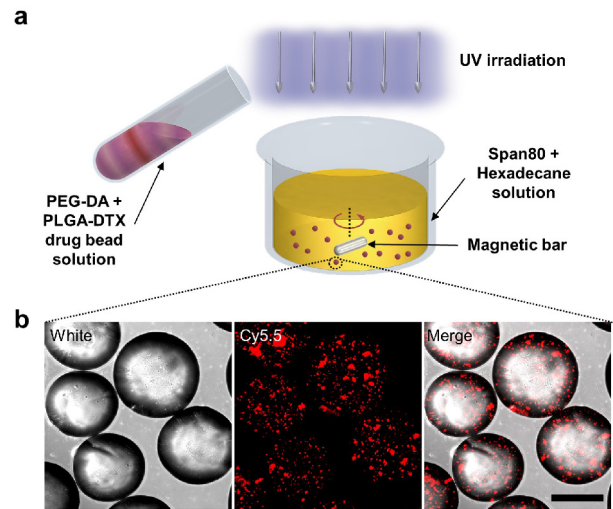


Fig. 3. (a) Schematic diagram of the fabrication of microbeads containing an anti-cancer drug. (b) Confocal microscopy images of the fabricated drug-containing microbeads. The scale bar represents 250 μm .

the microrobot is then made to unfold and open as the temperature is decreased ($T < T_{LCST}$). Finally, the micro-objects are released from the microrobot and delivered to the target (Fig. 1(d)).

As a demonstration of the feasibility of drug delivery using the microrobot, an in vitro drug delivery test was performed. For the in vitro test, a mouse mammary tumor cell line (4T1) was used, and microbeads encapsulating an anti-cancer drug were fabricated using the single emulsion method (Fig. 3(a)). The microbeads were composed of biocompatible PEGDA and poly(D,L-lactide-co-glycolide) (PLGA), and docetaxel (DTX) was used as the anti-cancer drug. The detailed cell culture and the fabrication process for the drug-loaded microbeads are presented in Section 3 (Materials and Methods). Fig. 3(b) shows a microscopy image of the fabricated PLGA-DTX nanoparticles encapsulated in spherical PEGDA microbeads of homogeneous size with a mean diameter of 300 μm (Fig. 3(b) - White). The encapsulation of the PLGA-DTX nanoparticles into the microbeads was confirmed by red fluorescence images (Fig. 3(b) - Cy5.5 and Merged).

3. MATERIALS AND METHODS

3.1. Materials

For microrobot fabrication, poly(ethylene glycol) diacrylate (average MW ≈ 700 , PEGDA), 2-hydroxy-2-methyl-propiofenone (97%, Darocur 1173), iron(II,III) oxide (< 50 nm), N-isopropylacrylamide monomer (99%, NIPAAm), N,N'-methylenebis-acrylamide (99.5%, BIS), phenylbis(2,4,6-trimethylbenzoyl)phosphine oxide (97%,

BAPO), trypan blue solution (0.4%), and Sigmacote (silane) were purchased from Sigma-Aldrich (St. Louis, MO). Methyl alcohol (99.8%) was provided by Duksan Pure Chemical (Kyungkido, Korea).

Next, for drug-containing microbead fabrication, PEGDA, Darocur 1173, Span 80, hexadecane, poly(D,L-lactide-co-glycolide) (MW \approx 30,000 - 60,000, PLGA), poly(vinyl alcohol) (MW \approx 61,000, PVA), dichloromethane (99.5%, DCM), and Rhodamine B were obtained from Sigma-Aldrich. Additionally, DTX was supplied by Jinhe Bio-Technology (Shanghai, China).

3.2. Microrobot fabrication

3.2.1 Synthesis of base solutions for bilayers

To obtain the Fe-PEGDA solution, PEGDA and Darocur 1173 at a mass ratio of 5.9:1 were dissolved in 800 μ L of deionized water. After mixing at 2500 rpm for 5 min, 10 wt% iron(II,III) oxide was added to the solution and dispersed using an ultrasonic agitator at 40 kHz for 2 h.

To form the NIPAAM solution, 120 mg of NIPAAM, 2.2 mg of BIS cross-linker and 1.5 mg of BAPO photoinitiator were dissolved in 210 μ L of methyl alcohol and 150 μ L of deionized water. Then, for NIPAAM hydrogel visualization, 20 μ L of trypan blue solution was added and mixed at 2500 rpm for 5 min.

3.2.2 Microrobot photo-patterning

The bilayer-structured microrobot was fabricated via two UV polymerization processes using 2D lithography (Fig. 2). The channels for the fabrication of the microrobot were prepared using two types of coverslips and double-sided tapes (Fig. 2(a), (d)). The thicknesses of each layer of the microrobot were determined by the different thicknesses of the double tapes (50 μ m and 300 μ m). Additionally, to prevent the loss of the desired layer during the removal of non-polymerized residue, the upper coverslip, which was subjected to UV irradiation, was given a non-adhesive surface through the application of a silane coating.

First, the Fe-PEGDA solution was injected by capillary force into the channel at a separation of 50 μ m. Once the photomask with the microrobot pattern was placed on top of the channel, the Fe-PEGDA solution was polymerized by UV light (365 nm, 25 mW/cm²) for 6 s (Fig. 2(b)). The silane-coated upper coverslip of the channel was then removed, and the non-polymerized Fe-PEGDA solution in the channel was washed away through the injection of additional deionized water (Fig. 2(c)). Next, for the UV polymerization of the NIPAAM solution, two double tapes (300 μ m) and a silane-coated upper coverslip were attached to the coverslip with the Fe-PEGDA layer. Similarly, the NIPAAM solution was introduced into the channel between the coverslips (Fig. 2(d)) and was exposed to UV light for 13 s. After removing the upper coverslip

and washing away the non-polymerized NIPAAM solution using additional methyl alcohol and deionized water, the pattern of the microrobot remained on the coverslip in a bilayer structure (Fig. 2(f)). Finally, by immersing the coverslip with the bilayered microrobot pattern in deionized water for 30 min, the microrobot itself was released from the coverslip (Fig. 2(g)).

3.3. Fabrication of drug-containing microbeads

3.3.1 Fabrication of PLGA-DTX nanoparticles

PLGA-DTX nanoparticles were prepared using the single emulsion method [32]. In brief, PLGA and docetaxel at a mass ratio of 10:1 were dissolved in 2 mL of DCM and vigorously mixed for 15 min. Then, the PLGA-DTX solution was added to 40 mL of PVA 1% to form an oil/water system under magnetic stirring. The oil/water (PLGA-DTX/PVA) system was emulsified via sonication (VC750, Sonics & Materials, Newton, CT) in an ice bath to form PLGA-DTX nanoparticles. After sonication, the system was continuously stirred for a further 8 h to allow the solvent to evaporate. Finally, the nanoparticles were washed three times with deionized water and were stored at 4 °C. To obtain fluorescence images, the fabricated nanoparticles, which contained carboxylic functional groups, were covalently linked to streptavidin PerCP-Cyanine5.5 (eBioscience, San Diego, CA).

3.3.2 Fabrication of PLGA-DTX nanoparticles encapsulated in PEGDA microbeads

Drug-containing microbeads (PEGDA-PLGA-DTX) were fabricated using the single emulsion method (Fig. 3a) [24]. In detail, 850 μ L of PEGDA (1.12 g/mL) was mixed with 150 μ L of Darocur (1.077 g/mL), 20 μ L of Rhodamine B (1 mg/mL), and PLGA-DTX nanoparticles under vigorous vortex mixing for 5 min. The oil-phase solution contained 5 mL of 15% Span 80 and 85% of hexadecane in a 10 mL beaker. Next, 150 μ L of the prepared PEGDA solution was poured into the oil-phase solution under stirring at 450 rpm. The solution was then exposed to UV at 356 nm and 0.45 W for 5 s to yield PEGDA-PLGA-DTX microbeads. Afterward, the microbeads were washed three times with deionized water and passed through a 300- μ m stainless steel filter to obtain microbeads of the desired sizes.

3.4. Cytotoxicity assay of the PEGDA-PLGA-DTX microbeads

The therapeutic effect of the PEGDA microbeads that contained PLGA-DTX nanoparticles, which were to be delivered by the fabricated microrobot, was evaluated via an MTT assay [33]. In brief, 100 μ L of 4T1 cells (105 viable cells per mL) were cultured in a 96-well plate (SPL Life Sciences) in Dulbecco's Modified Eagle's Medium (DMEM, Lonza, Walkersville, MD) in a humidified incubator for 24 h, and the cells were allowed to attach to the

bottoms of the wells. Afterward, the cells were treated with different amounts of DTX encapsulated in PEGDA-PLGA-DTX microbeads. After 24 h, the cells were washed again with PBS and incubated with 0.5 mg/mL MTT (Sigma-Aldrich) in DMEM for 3.5 h in the humidified incubator. The used medium was removed from each well, and the wells were refilled with an equivalent volume of dimethyl sulfoxide (DMSO). Finally, the viability of the cells was determined using a microplate reader set to measure at 570 nm.

3.5. Cell culture

Mammary carcinoma cells (4T1) were obtained from the American Type Culture Collection (Manassas, VA). The cells were cultured in DMEM containing 10% v/v FBS and 1% v/v antibiotic solution (Gibco-BRL/Invitrogen, Carlsbad, CA). The cells were maintained in an incubator at 37°C and 5% CO₂, dissociated in 0.5% trypsin-EDTA (Life Technologies, Grand Island, NY), and then centrifuged at 1200 rpm for 3 min. The resulting cell pellet was then suspended in DMEM [34].

3.6. Characterization of the electromagnetic actuation and thermal response actuation of the microrobot

The microrobot was characterized in terms of its magnetic and thermal response properties. The magnetic properties of the microrobot were evaluated by recording the magnetic hysteresis loops of three microrobot samples, which were measured using a vibrating sample magnetometer (VSM, Lake Shore Cryotronics 7404, USA).

The swelling ratios of the Fe-PEGDA and the NIPAAM hydrogel were investigated to characterize the thermal response properties of the microrobot. Disks of the Fe-PEGDA and the NIPAAM hydrogel (5 mm in diameter × 0.5 mm in thickness) were polymerized under UV irradiation and rinsed with deionized water. Five sample disks were immersed in deionized water and then dried for 6 h as the temperature was changed from 25°C to 60°C at 5°C intervals using a temperature controller (HB-502L, HAN-BAEK, South Korea). After removing the deionized water surrounding the samples, the weight of each disk was measured, and the mass swelling ratio (MSR) of the samples was calculated as follows [35, 36]:

$$MSR = \frac{M_w - M_d}{M_d}, \quad (5)$$

where M_w and M_d denote the swollen and dried weights of the samples, respectively.

The electromagnetic actuation performance of the microrobot was characterized based on the travel velocity of the microrobot. First, in the investigation of the pulling motion of the microrobot, the angular velocity (β in (1)) and oscillating angle (α in (1)) of the oscillating magnetic field were 0.5 rad/s and 90°, respectively. In addition, the current applied to the Helmholtz coils was fixed at 8 A,

and the current applied to the Maxwell coils was varied from 4 A to 8 A. Next, to investigate the rolling motion of the microrobot, a constant current (8 A) was applied to the three pairs of Helmholtz coils, and the frequency (ω in (2)) of the rotating magnetic field was increased from 1 Hz to 13 Hz.

The temperature change of the working fluid (deionized water) was measured to evaluate the thermal actuation performance of the microrobot. To transfer heat to the microrobot, a heating stage equipped with a Peltier element (FALC1-03180T150, OEM, China) was used. Additionally, a fiber-optic temperature probe (NY2, PhotoControl, Canada) was used to record the temperature of the deionized water. In the test, the deionized water was heated by the heating stage (operating at a constant voltage of 2 V) for approximately 60 s, and the water was then cooled to room temperature over approximately 150 s.

3.7. Electromagnetic and thermal control for microrobot manipulation

The locomotion of the microrobot and the operation of the heating stage were controlled under tele-operation using two joysticks and LabVIEW software (National Instruments, USA). One joystick was used for the locomotive direction control of the microrobot, and the other was used for the current control of the electromagnetic coils. The currents for the EMA system and the heating stage were applied using five power supply units (three MX15 units and two 3001iX units, AMETEK, USA). For the position recognition of the microrobot, a Digital Single Lens Reflex (DSLR) camera (EOS 600D, CANON, Japan) was installed. In addition, a fiber-optic probe was mounted to observe the temperature change of the working fluid.

3.8. Fabrication of the working chamber for the in vitro test

The working chamber for a drug delivery test using the microrobot was prepared as follows: First, a mold was fabricated by attaching a dumbbell-type structure, which was created using a 3D printer (Objet30 Pro, USA), to a glass substrate. Then, a PDMS prepolymer was prepared by mixing the PDMS precursor and the curing agent at a ratio of 10:1; the prepolymer was then poured into the mold. A PDMS block was fabricated by curing the PDMS prepolymer at 80°C for 1 h and then cutting it into a 22 mm × 40 mm rectangle. Finally, the working chamber was fabricated by attaching the PDMS block to a cover slip (22 mm in width × 40 mm in length × 100 μm in thickness) using O₂ plasma (Fig. 4). The fabricated working chamber was divided into two regions (the drug bead reservoir and the target area).

3.9. Experimental setup for the in vitro test

An in vitro test was conducted to evaluate the feasibility of drug delivery using the thermo-electromagnetically

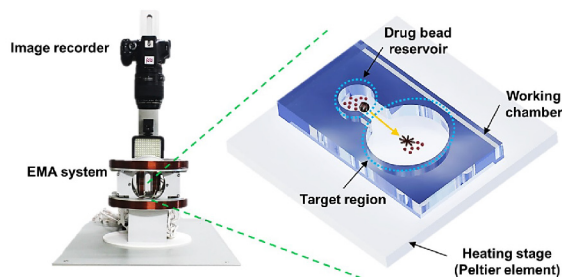


Fig. 4. Experimental setup for the in vitro test using the microrobot.

actuated microrobot. For the electromagnetic and thermal actuation of the microrobot, the working chamber in which the microrobot was to be operated was positioned in the ROI of the EMA system and placed on the heating stage. For clear visualization of the microrobot and the drug-containing microbeads, FluoroBrite™ DMEM (Life Technologies) without phenol red was used as the working fluid. To observe and record the locomotion and thermal activation of the microrobot, a DSLR camera was installed in an orthogonal orientation to the working chamber. A light source was also placed beside the EMA system to enhance image quality. After the delivery of the drug-loaded microbeads using the microrobot, the therapeutic effect of the microbeads loaded with the anti-cancer drug docetaxel was investigated using an optical microscope combined with a live cell imaging instrument (Live Cell Instrument, South Korea).

4. RESULTS AND DISCUSSION

4.1. Characterization of the microrobot

The thermo-electromagnetically actuated microrobot was characterized using various fundamental tests to probe the magnetic hysteresis loop, swelling properties, travel velocity, and shape changing behavior of the microrobot as a function of the temperature changes induced by the heating stage.

First, the magnetic properties of the microrobot were obtained using a vibrating sample magnetometer (VSM), in which external magnetic fields ranging from -1 T to 1 T were applied at room temperature to three microrobot samples (Fig. 5(a)). These samples exhibited similar magnetic hysteresis loops, with a saturation magnetization of 1.462 - 1.735 emu/g and a small coercivity of several milli-tesla. Based on these results, the loading level of iron(II,III) oxide in the microrobot was estimated from the expected and measured saturation magnetization values. Here, the expected saturation magnetization value (1.208 emu/g) of the microrobot was determined based on the specifications of the Fe-PEGDA layer of the microrobot, which contained 10 wt% iron(II,III) oxide, cor-

responding to a mass concentration of 1.51%; thus, the expected value was calculated from this mass concentration (1.51%) and the magnetic saturation value (80 emu/g) of pure iron(II,III) oxide. Consequently, it was confirmed that the measured saturation magnetization value differed slightly from the expected value, which may be attributed to inaccuracies in the fabrication process, such as inaccuracies in the thicknesses of the bilayers and the sizes and uniformity of the structures.

Second, the thermo-responsive swelling properties of the Fe-PEGDA and NIPAAM hydrogel layers were analyzed (Fig. 5(b)). The swelling ratio of the NIPAAM hydrogel was drastically decreased in a temperature range of 30 - 35°C , and the hydrogel was fully collapsed above 35°C , corresponding to the LCST of a typical NIPAAM hydrogel. Thus, the NIPAAM hydrogel was a suitable layer material for achieving the thermal actuation of the self-folding microrobot. In the case of the Fe-PEGDA, the swelling ratio remained constant as the temperature changed. Consequently, when the microrobot bilayer structure comprising Fe-PEGDA and the NIPAAM hydrogel was subjected to NIPAAM hydrogel shrinkage at temperatures above the LCST, the bilayer structure bent toward the NIPAAM hydrogel.

Third, the electromagnetic actuation performance of the microrobot was characterized in terms of the velocities of the two motions (pulling and rolling) of the microrobot. The travel velocity of the microrobot that could be achieved using the pulling motion varied from 0.338 mm/s to 0.529 mm/s as the current applied to the Maxwell coils was increased (Fig. 5(c) - Left). When the current applied to the Maxwell coils was less than 4 A, the microrobot did not move because of the frictional forces related to the microrobot's weight and the van der Waals force. Next, the travel velocity of the microrobot that could be achieved using the rolling motion was measured as a function of the frequency of the rotating magnetic field (Fig. 5(c) - Right). The rolling speed of the microrobot increased linearly in a frequency range from 1 Hz to 7 Hz, and the microrobot reached its maximum velocity of 5.007 mm/s at 7 Hz. At frequencies above 7 Hz, the velocity of the microrobot gradually decreased because the frequency of the rotating magnetic field became higher than the step-out frequency of the electromagnetically actuated microrobot [37]. These results revealed that the achievable travel velocities of the microrobot on a 2D plane using pulling and rolling motions depended on the current applied to the Maxwell coils and the frequency of the rotating magnetic field produced by the Helmholtz coils, respectively. The rolling motion of the microrobot yielded a velocity that was faster by a factor of 10 than that yielded by the pulling motion.

Fourth, we measured the change in the temperature of the working fluid (deionized water) of the microrobot that was induced by the heating stage (Fig. 5(d)). In this

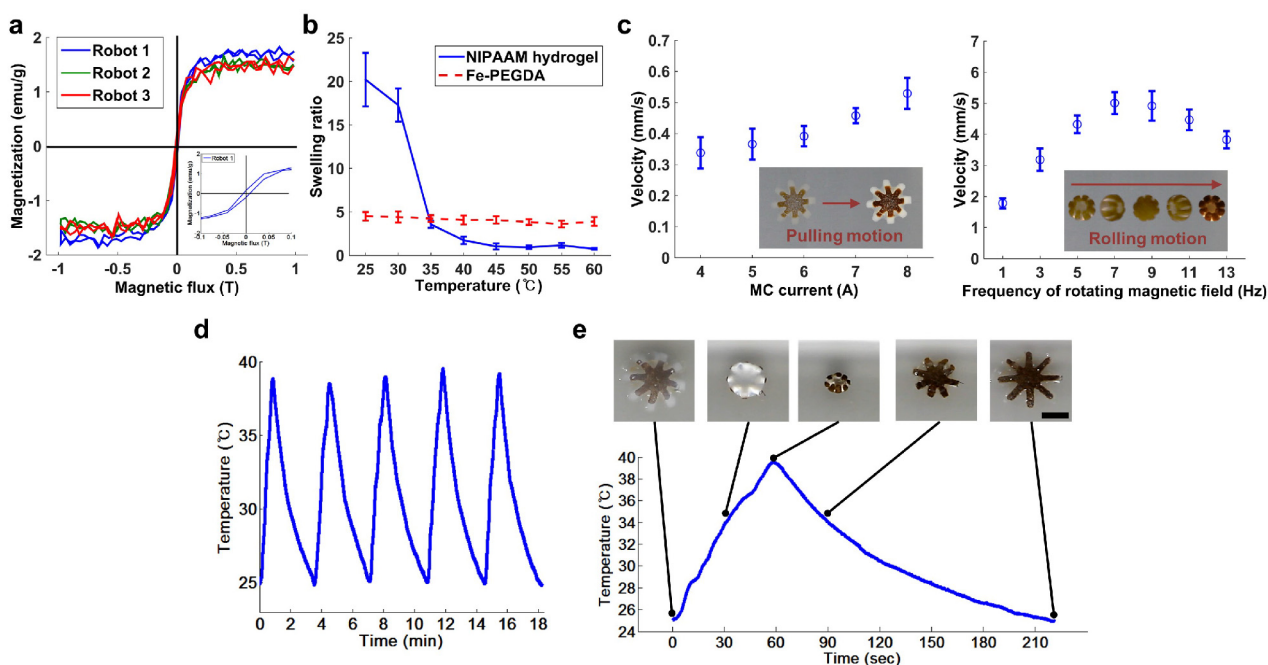


Fig. 5. Characterization of the microrobot. (a) Magnetization measurements of microrobot samples with iron(II,III) oxide powder. (b) Swelling ratios of the Fe-PEGDA and NIPAAAM hydrogel layers. (c) Velocity measurements of the microrobot while subjected to pulling and rolling motions, depending on the microrobot shape. (d) Temperature changes in response to the operation of the heating stage. (e) Optical images of the shape transition of the microrobot occurring in response to the change in temperature. The scale bar represents 1 mm.

test, we considered that deionized water should be very similar to the medium used in the *in vitro* test because that medium comprised greater than 95% deionized water. The temperature of the deionized water was increased to a maximum of 39.55°C during the operation of the heating stage (60 s) and was decreased to room temperature (25°C) during a cooling time of approximately 150 s. The maximum temperature (39.55°C) of the deionized water during the heating operation was higher than the LCST of the NIPAAAM hydrogel. Thus, when heating was applied to the microrobot, its shape could be changed as a result of the swelling and shrinkage of the NIPAAAM hydrogel layer. Moreover, the maximum temperature (39.55°C) remained lower than the trigger temperature (42–44°C) for cellular heat shock proteins (HSPs), the release of which indicates cellular protein deformation at high temperatures [38, 39]. Therefore, when the heating stage was used in the *in vitro* test for drug delivery, no cellular protein deformation was induced by the applied heat. In addition, the temperature changes in the deionized water over five heating and cooling cycles exhibited nearly identical patterns to those of the first heating and cooling cycle. Thus, the thermal actuation of the microrobot achieved through the operation of the heating stage was highly repeatable.

Finally, we observed the shape transition of the microrobot as a function of the temperature change controlled using the heating stage (Fig. 5(e)). The micro-

robot presented an unfolded shape at the initial temperature (25°C) and began to fold as the temperature was increased by the operation of the heating stage. The microrobot was approximately 50% folded at the LCST (35°C) of the NIPAAAM hydrogel and was fully folded and closed at approximately 40°C. During the heating cycle, the microrobot exhibited a white color due to the collapse of the polymer chains in the NIPAAAM hydrogel [14]. As the temperature was decreased, the NIPAAAM hydrogel of the microrobot became transparent due to the absorption of deionized water, and the microrobot unfolded and opened. Based on these results, we expect that micro-objects smaller than the microrobot can be trapped, delivered and released using the self-folding microrobot.

4.2. Microbead trapping, delivery, and release test using the microrobot

As a proof of concept, we demonstrated the trapping, delivery, and release of a polystyrene microbead (250 μm) using a thermo-electrically actuated microrobot controlled under tele-operation (Fig. 6 and Supplementary Material Video S1). First, the unfolded microrobot was guided to the microbead using a pulling motion. As the microrobot was positioned near the microbead and heated by the heating stage, the microrobot began to fold, trapping the microbead at approximately 39°C. The microrobot with the trapped microbead was then freely moved along the de-

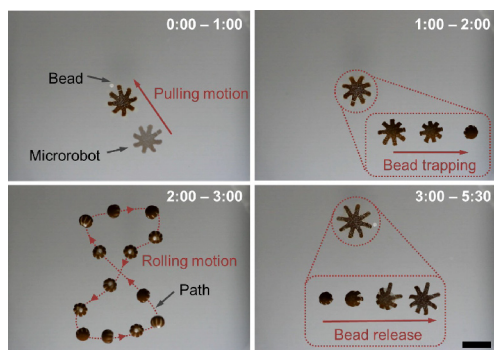


Fig. 6. Microbead manipulation (trapping, delivery, and release) using the microrobot under tele-operated control. The scale bar represents 2 mm. The time is indicated on each figure in the minutes:seconds format. A video of the actuation is provided in Supplementary Material Video S1.

sired path using a rolling motion. Here, to prevent unintended release of the microbead from the microrobot, we maintained the working fluid at a constant temperature of 39°C during the delivery locomotion of the microrobot. Finally, as the working fluid was cooled, the microrobot began to unfold and open, releasing the trapped microbead.

In addition, similar to the tele-operated test described above, we performed an autonomous control test of the microrobot, in which the microrobot carried and released the microbead under real-time visual tracking (Supplementary Material Video S2). In this test, the microrobot could autonomously track along 15 pre-defined points (Fig. 7). As a result, through feedback control based on position recognition, the thermo-electromagnetically actuated microrobot could not only trap the desired microbead but also deliver (transport) and release the microbead to the target area. In the future work, we expect that more precise and accurate thermal and magnetic actuation of the microrobot is possible by introducing tactile and haptic sensors capable of capturing multiple properties instead of teleoperation control using the joystick [40–42].

4.3. In vitro test: tumor therapy using the microrobot

As a potential biomedical application of the thermo-electromagnetically actuated microrobot, we conducted an in vitro drug delivery test for cancer therapy (Fig. 8(a), (b) and Supplementary Material Video S3). To deliver drug-containing microbeads from a reservoir to a target region, the microrobot was manipulated using the EMA system; the delivery process for the drug-containing microbeads can be described as follows (Fig. 8(a) and Supplementary Material Video S3). First, the microrobot was loaded into the working chamber and moved via a pulling motion into the reservoir of drug-containing mi-

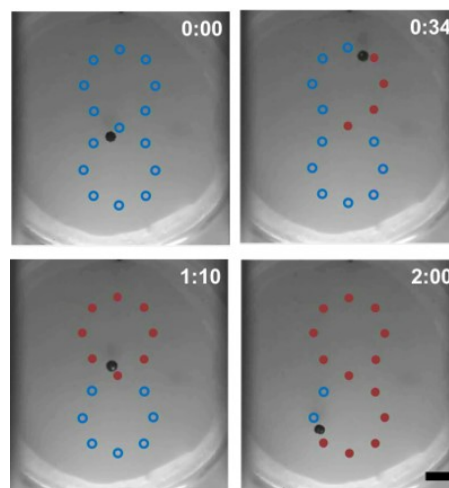


Fig. 7. Microbead manipulation using the microrobot under autonomous control using real-time visual tracking. This figure shows the microbead transport performed by the microrobot along a pre-selected pattern. The entire manipulation process, in which the microrobot traps, carries, and releases the microbead, is shown in Supplementary Material Video S2. The scale bar represents 3 mm. The time is indicated on each figure in the minutes:seconds format.

crobeads, where it trapped several microbeads (three to five microbeads were trapped in a single trapping motion). Then, the drug-containing microbeads were carried by the rolling microrobot to the tumor cells and released. As a result, a total of 11 drug-containing microbeads were delivered through four repeated operations of the microrobot. One of these four operations failed due to inaccurate positioning of the microrobot under tele-operated control.

The therapeutic effect of the drug-containing microbeads against the cancer cells was evaluated using live cell imaging. Specifically, immediately after the drug-containing microbeads were released from the microrobot to the cancer cells, the morphologies of the cancer cells and the microbeads were recorded; this time point was designated as 0 h. The morphologies were recorded again after 24 h (Fig. 8(b) and Supplementary Material Video S3). As a control, the same procedure was repeated using microbeads that were not loaded with the anti-cancer drug (Fig. 8(d)). The drug-containing microbeads that were delivered by the microrobot exerted an obvious therapeutic effect against the 4T1 cells, resulting in a drastic change in the morphologies of the cells after 24 h (Fig. 8(b)). By contrast, without the anti-cancer drug being present in the microbeads, the microbeads and the microrobot exhibited no cytotoxicity toward the cells and did not result in cell death (Fig. 8(d)). The cytotoxicities measured as a function of various drug concentrations in the drug-containing

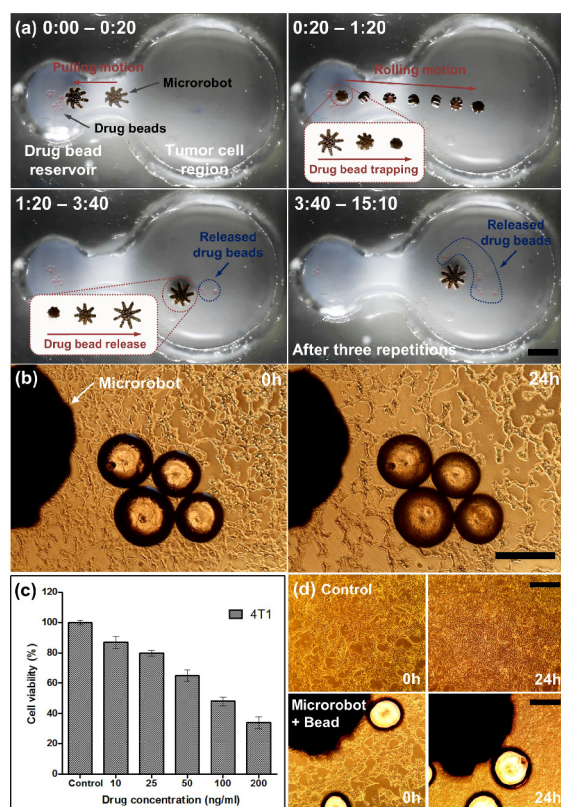


Fig. 8. Results of an in vitro test using the thermo-electromagnetically actuated microrobot. (a) Transport of the drug beads from the reservoir to the target region using the microrobot. The scale bar represents 3 mm. The time is indicated on each figure in the minutes:seconds format. (b) Optical micrographs of the cells and drug-containing microbeads at 0 h and 24 h. The scale bar represents 300 μm . (c) Cell viability as a function of drug concentration. (d) The morphologies of the microbeads without drug encapsulation and those of the cells treated with the microbeads at 0 h and 24 h. The scale bar represents 300 μm . A video of the actuation is presented in Supplementary Material Video S3.

microbeads reveal that the viability of the 4T1 cells decreased as the drug concentration was increased from 10 ng/mL to 200 ng/mL (Fig. 8(c)). The drug concentration required to kill $50 \pm 5\%$ of the 4T1 cells was 100 ng/mL. These results confirmed the successful delivery of the therapeutic agents (PEGDA-PLGA-DTX microbeads) by the microrobot to the 4T1 cancer cells.

4.4. Discussion

In this work, we proposed the targeted transport of therapeutic agents using a thermo-electromagnetically actuated microrobot. Most of the existing researches focused

on the characterization of the shape of microrobot by temperature change, but the magnetic actuation of the microrobot was not clearly characterized [14, 16, 17]. In addition, previous microrobots only showed a simple magnetic actuating motion using a gradient magnetic field regardless of the environment and the shape of the microrobot. On the other hand, we presented the characteristics of the shape of the microrobot by the temperature change as well as its magnetic actuating response through the velocity and magnetization curve. Also, according to its shape by temperature change, two motions such as pulling and rolling motions were assigned to the microrobot so that the microrobot can freely move by the two motions. Finally, unlike previous studies that only show the therapeutic effects of the microrobot without hybrid actuation, we demonstrated in-vitro test to show the performance of the hybrid (thermal and electromagnetic)-actuated microrobot and a therapeutic effect following drug delivery.

Some drug leakage occurred during bead transportation using the microrobot because some of the drug encapsulated in the beads released by diffusion. Thus, although the drug-containing beads are protected by the folded microrobot, the released drug can pass through the hydrogel body of the microrobot before reaching the target. In existing drug delivery systems using a passive targeting strategy [43, 44], drug-loaded beads circulate in the biological system and accumulate in the target via an enhanced permeation and retention effect (EPR). However, the proposed microrobot with active locomotion can deliver the therapeutic agents to the target without extended circulation time in the blood system. Therefore, the transport of therapeutic agents using the magnetic actuated microrobot can reduce premature drug leakage, increase the targeting ability, and achieve a good therapeutic effect. In addition, we performed an in vitro test to verify the delivery of the therapeutic agents using the proposed microrobot and to confirm the therapeutic effect (Fig. 7). In this test, the transport of 11 drug-containing beads required approximately only 15 minutes. According to a test of the in vitro controlled release of free DTX, only 1.25% of DTX is released within 15 minutes [45]. Additionally, we expect that DTX encapsulated by PEGDA and PLGA is released more slowly than free DTX. For this reason, premature drug release during the transport of drug-containing beads has little effect.

However, several shortcomings should be addressed before the microrobot is used in biomedical applications. First, the microrobot, which is composed of a NIPAAm hydrogel with an LCST of 35°C , will maintain its folding shape at biological temperatures (approximately 36.5°C). Thus, it would be difficult to utilize the thermal actuation function of the microrobot in a biological environment. As a solution to the problem of the low LCST of the NIPAAm hydrogel, the LCST of this material can be increased to greater than biological temperatures

through copolymerization with other monomers. For example, when acrylamide (AAM), hydroxymethylacrylamide (HMAAm), and dimethylacrylamide (DMAAm) are combined with the NIPAAM monomer, the resulting NIPAAM copolymers have LCSTs (39-41°C) that are higher than biological temperatures [19, 46]. Therefore, a microrobot composed of a hydrogel consisting of NIPAAM copolymerized with other monomers (AAM, HMAAm, and DMAAm) and Fe-PEGDA could maintain its unfolded shape at biological temperatures. Such a microrobot could then be thermally actuated and folded in the biological environment through the application of external stimuli [16, 17], such as near-infrared light and an alternating magnetic field. In addition, we expected that a microrobot with a trigger temperature above that of the biological environment could usefully be applied in medical applications. First, the microrobot grips the therapeutic agents in a reservoir and is injected into the biological environment. After the injection of the microrobot, the microrobot maintains its folded shape through an external stimulus and delivers the therapeutic agent to the target region. When the temperature is decreased by removing the applied external stimulus, the microrobot opens, and the therapeutic agent is released at the target site. Second, because of the relatively large size of the microrobot used in this work, it would be difficult for this microrobot to pass through a narrow capillary vessel. This microrobot was fabricated as a prototype to test the feasibility of the design for use in biomedical applications. In future work, by applying improved MEMS technology in the microrobot fabrication process, we will scale down the size of the microrobot for use in biomedical applications.

5. CONCLUSION

In summary, we present a method for the targeted transport of therapeutic agents using a hybrid actuated microrobot. The bilayer-structured microrobot can be made to undergo self-folding by exploiting the thermal response of a NIPAAM hydrogel, and targeted positioning can be achieved through the electromagnetic actuation capability provided by Fe-PEGDA. Using these properties, the microrobot can trap, deliver, and release microbeads. In particular, pulling and rolling motions can be applied by electromagnetic actuation to the microrobot while in its unfolded and folded shapes, respectively. Through fundamental experiments, the performance of the microrobot was evaluated in terms of its magnetization curve, swelling ratio, travel velocity, and shape changing behavior. Due to its characteristics, polystyrene beads could be manipulated using the microrobot. Finally, an in vitro test for tumor therapy using the microrobot was demonstrated. Prior to the in vitro test, drug-encapsulating microbeads (PEGDA-PLGA-DTX) were fabricated. These drug-carrying microbeads were then delivered to tumor

cells by the microrobot, and the delivered microbeads exhibited therapeutic effects on the tumor cells. This in vitro test demonstrated that targeted drug delivery is achievable using the microrobot. Through these experiments, we verified the proposed concept and demonstrated that the microrobot performed well under hybrid actuation. Consequently, we expect that this thermo-electromagnetically actuated microrobot can also be used to transport other therapeutic objects, such as specific drugs, stem cells and immune cells to target regions. In addition, we envision that the microrobot can be utilized in various biomedical applications.

REFERENCES

- [1] B. J. Nelson, I. K. Kaliakatsos, and J. J. Abbott, "Microrobots for minimally invasive medicine," *Annual Review of Biomedical Engineering*, vol. 12, pp. 55-85, 2010. [click]
- [2] K. E. Peyer, L. Zhang, and B. J. Nelson, "Bio-inspired magnetic swimming microrobots for biomedical applications," *Nanoscale*, vol. 5, no. 4, pp. 1259-1272, 2013. [click]
- [3] M. Sitti, H. Ceylan, H. Wenqi, J. Giltinan, M. Turan, S. Yim, and E. Diller, "Biomedical applications of untethered mobile milli/microrobots," *Proceedings of the IEEE*, vol. 103, no. 2, pp. 205-224, 2015. [click]
- [4] J. D. Keuning, J. de Vriesy, L. Abelmanny, and S. Misra, "Image-based magnetic control of paramagnetic microparticles in water," *Proc. of IEEE/RSJ International Conference on Intelligent Robots and Systems (IROS)*, pp. 421-426, 2011.
- [5] H. Choi, K. Cha, S. Jeong, J. Park, and S. Park, "3-D locomotive and drilling microrobot using novel stationary EMA system," *IEEE/ASME Transactions on Mechatronics*, vol. 18, no. 3, pp. 1221-1225, 2013. [click]
- [6] M. T. Hou, H. M. Shen, G. L. Jiang, C. N. Lu, I. J. Hsu, and J. A. Yeh, "A rolling locomotion method for untethered magnetic microrobots," *Applied Physics Letters*, vol. 96, no. 2, pp. 024102, 2010. [click]
- [7] E. Diller and M. Sitti, "Three-dimensional programmable assembly by untethered magnetic robotic micro-grippers," *Advanced Functional Materials*, vol. 24, no. 28, pp. 4397-4404, 2014. [click]
- [8] A. W. Mahoney, J. C. Sarrazin, E. Bamberg, and J. J. Abbott, "Velocity control with gravity compensation for magnetic helical microswimmers," *Advanced Robotics*, vol. 25, no. 8, pp. 1007-1028, 2011. [click]
- [9] P. Mandal, V. Chopra, and A. Ghosh, "Independent positioning of magnetic nanomotors," *ACS Nano*, vol. 9, no. 5, pp. 4717-4725, 2015.
- [10] I. S. M. Khalil, H. C. Dijkslag, L. Abelmann, and S. Misra, "MagnetoSperm: a microrobot that navigates using weak magnetic fields," *Applied Physics Letters*, vol. 104, no. 22, pp. 223701, 2014. [click]

- [11] K. Youakim, M. Ehab, O. Hatem, S. Misra, and I. S. M. Khalil, "Paramagnetic microparticles sliding on a surface: Characterization and closed-loop motion control," *Proc. of IEEE International Conference on Robotics and Automation (ICRA)*, pp. 4068-4073, 2015. [click]
- [12] C. Pawashe, S. Floyd, and M. Sitti, "Modeling and experimental characterization of an untethered magnetic microrobot," *The International Journal of Robotics Research*, vol. 28, no. 8, pp. 1077-1094, 2009.
- [13] J. Li, T. Li, T. Xu, M. Kiristi, W. Liu, Z. Wu, and J. Wang, "Magneto-acoustic hybrid nanomotor," *Nano Letters*, vol. 15, no. 7, pp. 4814-4821, 2015. [click]
- [14] J. C. Breger, C. Yoon, R. Xiao, H. R. Kwag, M. O. Wang, J. P. Fisher, T. D. Nguyen, and D. H. Gracias, "Self-folding thermo-magnetically responsive soft microgrippers," *ACS Appl Mater Interfaces*, vol. 7, no. 5, pp. 3398-3405, 2015. [click]
- [15] E. Diller, N. Zhang, and M. Sitti, "Modular micro-robotic assembly through magnetic actuation and thermal bonding," *Journal of Micro-Bio Robotics*, vol. 8, no. 3-4, pp. 121-131, 2013.
- [16] S. Fusco, M. S. Sakar, S. Kennedy, C. Peters, R. Bottani, F. Starsich, A. Mao, G. A. Sotiriou, S. Pane, S. E. Pratsinis, D. Mooney, and B. J. Nelson, "An integrated micro-robotic platform for on-demand, targeted therapeutic interventions," *Advanced Materials*, vol. 26, no. 6, pp. 952-957, 2014.
- [17] J.-C. Kuo, H.-W. Huang, S.-W. Tung, and Y.-J. Yang, "A hydrogel-based intravascular microgripper manipulated using magnetic fields," *Sensors and Actuators A: Physical*, vol. 211, pp. 121-130, 2014.
- [18] S. Miyashita, S. Guitron, M. Ludersdorfer, C. R. Sung, and D. Rus, "An untethered miniature origami robot that self-folds, walks, swims, and degrades," *Proc. of IEEE International Conference on Robotics and Automation (ICRA)*, pp. 1490-1496, 2015. [click]
- [19] S. N. Tabatabaei, J. Lapointe, and S. Martel, "Shrinkable hydrogel-based magnetic microrobots for interventions in the vascular network," *Advanced Robotics*, vol. 25, no. 8, pp. 1049-1067, 2011. [click]
- [20] D. Li, H. Choi, S. Cho, S. Jeong, Z. Jin, C. Lee, S. Y. Ko, J. O. Park, and S. Park, "A hybrid actuated microrobot using an electromagnetic field and flagellated bacteria for tumor-targeting therapy," *Biotechnology and Bioengineering*, vol. 112, no. 8, pp. 1623-1631, 2015. [click]
- [21] V. Magdanz, S. Sanchez, and O. G. Schmidt, "Development of a sperm-flagella driven micro-bio-robot," *Advanced Materials*, vol. 25, no. 45, pp. 6581-6588, 2013. [click]
- [22] I. S. Khalil, V. Magdanz, S. Sanchez, O. G. Schmidt, and S. Misra, "Wireless magnetic-based closed-loop control of self-propelled microjets," *PLoS One*, vol. 9, no. 2, pp. e83053, 2014. [click]
- [23] A. A. Solovev, Y. Mei, E. Bermudez Urena, G. Huang, and O. G. Schmidt, "Catalytic microtubular jet engines self-propelled by accumulated gas bubbles," *Small*, vol. 5, no. 14, pp. 1688-1692, 2009.
- [24] S. Cho, S. J. Park, S. Y. Ko, J. O. Park, and S. Park, "Development of bacteria-based microrobot using biocompatible poly(ethylene glycol)," *Biomed Microdevices*, vol. 14, no. 6, pp. 1019-25, 2012.
- [25] V. Nerapusri, J. L. Keddie, B. Vincent, and I. A. Bushnak, "Swelling and deswelling of adsorbed microgel monolayers triggered by changes in temperature, pH, and electrolyte concentration," *Langmuir*, vol. 22, no. 11, pp. 5036-5041, 2006. [click]
- [26] C. Yu, Y. Pan, H. Ma, T. Ma, J. Zhang, Y. Song, M. Y. Kalani, L. Dai, and H. Jiang, "Thermoresponsiveness of integrated ultra-thin silicon with poly (N-isopropylacrylamide) hydrogels," *Macromolecular rapid communications*, vol. 32, no. 11, pp. 820-824, 2011.
- [27] G. Go, H. Choi, S. Jeong, S. Y. Ko, J. Park, and S. Park, "Selective microrobot control using a thermally responsive microclasper for microparticle manipulation," *Smart Materials and Structures*, vol. 25, no. 3, pp. 035004, 2016.
- [28] H. Choi, J. Choi, G. Jang, J. Park, and S. Park, "Two-dimensional actuation of a microrobot with a stationary two-pair coil system," *Smart Materials and Structures*, vol. 18, no. 5, pp. 055007, 2009.
- [29] S. Jeong, H. Choi, K. Cha, J. Li, J. Park, and S. Park, "Enhanced locomotive and drilling microrobot using precessional and gradient magnetic field," *Sensors and Actuators A: Physical*, vol. 171, no. 2, pp. 429-435, 2011. [click]
- [30] S. Floyd, C. Pawashe, and M. Sitti, "Two-dimensional contact and noncontact micromanipulation in liquid using an untethered mobile magnetic microrobot," *IEEE Transactions on Robotics*, vol. 25, no. 6, pp. 1332-1342, 2009. [click]
- [31] U. K. Cheang, F. Meshkati, D. Kim, M. J. Kim, and H. C. Fu, "Minimal geometric requirements for micropropulsion via magnetic rotation," *Physical Review E*, vol. 90, no. 3, pp. 033007, 2014. [click]
- [32] C. G. Keum, Y. W. Noh, J. S. Baek, J. H. Lim, C. J. Hwang, Y. G. Na, S. C. Shin, and C. W. Cho, "Practical preparation procedures for docetaxel-loaded nanoparticles using polylactic acid-co-glycolic acid," *International Journal of Nanomedicine*, vol. 6, pp. 2225-34, 2011. [click]
- [33] M. S. Muthu, S. A. Kulkarni, J. Xiong, and S. S. Feng, "Vitamin E TPGS coated liposomes enhanced cellular uptake and cytotoxicity of docetaxel in brain cancer cells," *International Journal of Pharmaceutics*, vol. 421, no. 2, pp. 332-340, 2011.
- [34] S. J. Park, S. H. Park, S. Cho, D. M. Kim, Y. Lee, S. Y. Ko, Y. Hong, H. E. Choy, J. J. Min, J. O. Park, and S. Park, "New paradigm for tumor theranostic methodology using bacteria-based microrobot," *Scientific reports*, vol. 3, pp. 1-8, 2013.
- [35] C.-W. Lo, D. Zhu, and H. Jiang, "An infrared-light responsive graphene-oxide incorporated poly(N-isopropylacrylamide) hydrogel nanocomposite," *Soft Matter*, vol. 7, no. 12, pp. 5604-5609, 2011.
- [36] N. S. Satarkar and J. Z. Hilt, "Magnetic hydrogel nanocomposites for remote controlled pulsatile drug release," *Journal of Controlled Release*, vol. 130, no. 3, pp. 246-251, 2008. [click]

- [37] A. W. Mahoney, N. D. Nelson, K. E. Peyer, B. J. Nelson, and J. J. Abbott, "Behavior of rotating magnetic microrobots above the step-out frequency with application to control of multi-microrobot systems," *Applied Physics Letters*, vol. 104, no. 14, pp. 144101, 2014. [click]
- [38] P. Ginet, K. Montagne, S. Akiyama, A. Rajabpour, A. Taniguchi, T. Fujii, Y. Sakai, B. Kim, D. Fourmy, and S. Volz, "Towards single cell heat shock response by accurate control on thermal confinement with an on-chip microwire electrode," *Lab Chip*, vol. 11, no. 8, pp. 1513-1520, 2011. [click]
- [39] S. Wang, K. R. Diller, and S. J. Aggarwal, "Kinetics study of endogenous heat shock protein 70 expression," *International Mechanical Engineering Congress and Exposition*, vol. 125, no. 6, pp. 794-797, 2003.
- [40] H. Liu, F. Sun, D. Guo, B. Fang, and Z. Peng, "Structured output-associated dictionary learning for haptic understanding," *IEEE Transactions on Systems, Man, and Cybernetics: Systems*, vol. 47, no. 7, pp. 1564-1574, 2017. [click]
- [41] H. Liu, Y. Yu, F. Sun, and J. Gu, "Visual-tactile fusion for object recognition," *IEEE Transactions on Automation Science and Engineering*, vol. 14, no. 2, pp. 996-1008, 2017. [click]
- [42] H. Liu, D. Guo, and F. Sun, "Object recognition using tactile measurements: kernel sparse coding methods," *IEEE Transactions on Instrumentation and Measurement*, vol. 65, no. 3, pp. 656-665, 2016. [click]
- [43] H. Maeda, H. Nakamura, and J. Fang, "The EPR effect for macromolecular drug delivery to solid tumors: improvement of tumor uptake, lowering of systemic toxicity, and distinct tumor imaging in vivo," *Advanced drug delivery reviews*, vol. 65, no. 1, pp. 71-79, 2013. [click]
- [44] V. Torchilin, "Tumor delivery of macromolecular drugs based on the EPR effect," *Advanced Drug Delivery Reviews*, vol. 63, no. 3, pp. 131-135, 2011. [click]
- [45] S. Zheng, Z. Jin, J. Han, S. Cho, V. D. Nguyen, S. Y. Ko, J. Park, and S. Park, "Preparation of HIFU-triggered tumor-targeted hyaluronic acid micelles for controlled drug release and enhanced cellular uptake," *Colloids and Surfaces B: Biointerfaces*, vol. 143, pp. 27-36, 2016. [click]
- [46] C. Oerlemans, W. Bult, M. Bos, G. Storm, J. F. Nijssen, and W. E. Hennink, "Polymeric micelles in anticancer therapy: targeting, imaging and triggered release," *Pharmaceutical Research*, vol. 27, no. 12, pp. 2569-2589, 2010. [click]



Gwangjun Go received his B.S. (2013) and M.S. (2015) degrees from the Department of Mechanical Engineering at Chonnam National University, Korea. Currently, he is a researcher in the Robot Research Initiative (RRI). His research interests are micro/nanorobots.



Van Du Nguyen received his Master's degree of Science in Industrial & Systems Engineering from Korea Advanced Institute of Science and Technology (KAIST), Korea in 2009. In 2014, he joined the Robot Research Initiative, School of Mechanical Engineering, Chonnam National University, Korea as a Ph.D. student. His research interests include biomedical micro/nano robots, targeted drug delivery systems.



Jin Zhen received his B.S. (2012) degree from the department of Mechanical Engineering at Yanbian University of Science and Technology (YUST), China. Currently, he is a Ph.D. candidate in Chonnam National University and a researcher in Robot Research Initiative (RRI). His research interests are micro/nanorobots, high focused ultrasound (HIFU), and drug

delivery system.



Jong-Oh Park received his B.S. (1978) and M.S. (1981) degrees from the Department of Mechanical Engineering, Korea, and his Ph.D. (1987) in robotics from Stuttgart University, Germany. From 1982 to 1987, he worked as a guest researcher at Fraunhofer-Gesellschaft Institut für Produktionstechnik und Automatisierung (FhG IPA), Germany. He worked as a principal researcher at Korea Institute of Science and Technology (KIST) from 1987 to 2005 and he was a director of the Microsystem Research Center at KIST from 1999 to 2005. In 2005, he moved to Chonnam National University, where he is now a full professor in the Department of Mechanical System Engineering and a director of the Robot Research Initiative (RRI). His research interests are biomedical microrobots, medical robots, and service robots.



Sukho Park earned his Master's degree (1995) and Ph.D. (2000) in Mechanical Engineering from Korea Advanced Institute of Science and Technology (KAIST), Korea. From 2000 to 2004, he worked as a senior research engineer at LG Electronics Production Research Center, Korea. From 2004 to 2006, he worked as a senior researcher of Microsystem Research Center in the Korea Institute of Science and Technology. From 2006 to 2016, he worked as a professor of the School of Mechanical Engineering in Chonnam National University and a section head of the robot research initiative (RRI). In 2017, he moved to Daegu Gyeongbuk Institute of Science and Technology (DGIST), where he is now a full professor in Department of Robotics Engineering. His research interests are microactuator/robot and micromanipulation for biomedical instrumental applications.